Advances in Science and Technology
Research Journal

Advances in Science and Technology Research Journal, 2025, 19(11), 189–205
https://doi.org/10.12913/22998624/208869
ISSN 2299-8624, License CC-BY 4.0

Received: 2025.07.10
Accepted: 2025.09.15
Published: 2025.10.01

Experimental and numerical analysis of contact stresses in a single-lap riveted joint with a blind rivet

Monika Lubas[1]

[1] Department of Aerospace Engineering Faculty of Mechanical Engineering and Aeronautics,
Rzeszow University of Technology, Rzeszow, Poland
E-mail: m.lubas@prz.edu.pl

ABSTRACT

The article presents an experimental and numerical analysis of the influence of the hole chamfer size of a single lap joint with a blind rivet on contact stresses. The rivet–hole interface is critical due to the presence of secondary bending, stress concentration, shear stress, and local plastic deformation. To better understand the deformation and failure mechanisms, cross-sectional views of riveted joints under different loads were examined. Contact stresses were also analyzed using the classical Hertzian model, which, while useful under idealized conditions, fails to account for complex geometry and material nonlinearity. A modified version of the Hertz model was therefore proposed, incorporating geometric corrections based on the chamfer size and angle. The research object was a single-lap riveted joint made by the ISO 12996 standard, modeled using a discrete riveted model and nonlinear material properties. Different hole chamfer size configurations and various load cases were considered in the analyses to better illustrate the relationship between the numerical and experimental results. Contact stresses and stress distribution in the riveted joint cross-section were analyzed. Results showed that increasing the chamfer depth significantly affects the distribution of contact stresses and improves rivet forming as well as load capacity, although it also increases the risk of localized overloading. A strong qualitative agreement was found among experimental data, numerical analysis, and the modified analytical model. The research demonstrates the effectiveness of a hybrid analytical-numerical approach for accurately evaluating stress behavior in riveted joints under complex loading conditions.

Keywords: blind rivet, capacity, chamfer size, contact stress, Hertz model.

INTRODUCTION

The analysis of contact stresses is a key issue in mechanics and engineering, with significant importance for the design and evaluation of the strength of various structural elements [1, 2, 3]. These stresses, contact stresses, occur in the areas where two or more bodies come into contact under the influence of external loads [4], and their accurate determination is essential for predicting the operational reliability of machines and structures [5]. The analysis of contact stresses is applied in many fields, primarily in mechanics. Contact stress evaluation is common in bolted and riveted joints [6], but also applies to bearings, cutting tool interfaces, and biomedical implants. Contact stress behavior is influenced by several factors, including geometry [7, 8], material properties, and surface conditions. For example, Chang et al. [9] proposed a hybrid FT-FEM method to model bolted joints by capturing micro- and macro-contact effects, showing improvements in stiffness and vibration resistance. Material-related parameters such as Young's modulus, yield strength, and viscoelasticity [10], as well as surface roughness and micro-asperities as well as frictional interactions between contact surfaces affect the wear of components [11, 12], significantly affect contact stiffness and wear behavior [13]. Wang et al. [14] introduced a fractal stiffness model that includes asperity interaction and deformation, while thin coatings and films further complicate elastoplastic behavior in contact regions [15]. External load characteristics and boundary conditions also play critical roles in stress distribution [16]. Hertzian-based models, such as those enhanced by Flores et al. [17], incorporate hysteretic damping to address energy loss during contact. Similarly, new numerical techniques for contact analysis, such as the method proposed in [18], improve the simulation of deformation and force transmission in flexible mechanisms.

Analytical methods, including classical Hertz theory, are useful for simple geometries and elastic materials [1, 19]. For example, Guo et al. [20] introduced a modified Hertz model to predict stress under spherical indentations in soft materials, while Skrinjar et al. [21] analyzed the performance of various contact models, including hysteresis effects. Askari [22] explored non-Hertzian alternatives for more realistic scenarios. However, real-world applications often involve complex geometries and nonlinearities that analytical solutions cannot capture. Experimental methods remain essential for validating theoretical and numerical approaches [23], particularly in assessing contact wear and deformation [24] as well as the nature of contact, such as penetration, sliding, etc. Mohs and Tobi [25] examined tribological wear in Ti-6Al-4V alloys under various slip conditions. Their study compared finite element simulations with observed wear patterns and fatigue crack initiation, emphasizing the relevance of experimental validation.

Riveted joints are widely used in many industries. Accurate contact stress modeling is essential for understanding their load-bearing behavior, enabling optimized design and minimizing failure risk. Numerical methods, particularly the finite element method (FEM), are widely applied to analyze complex contact phenomena, including nonlinearities, contact stiffness [26], plasticity [27], and friction [28]. In the study [29], FEM was used to simulate surface microcompression in thermal barrier coatings (TBC) produced via atmospheric plasma spraying (APS). The study showed that porosity significantly affects stress distribution, force-displacement characteristics, and plastic deformation behavior beneath the contact area.

There are many factors influencing the distribution and magnitude of contact stresses in riveted joints. In work [30], a numerical analysis of the rivet shank upsetting process was conducted, with results compared to analytical estimates for a freely upset cylinder. Szymczyk and Jachimowicz [31] analyzed the damage caused by cyclic tension in lap joints, using FEM simulations of the riveting process and joint loading, complemented by static/fatigue tests and fractographic analysis. A critical factor is the material used for the rivet and connected components, particularly their mechanical properties such as Young's modulus and yield strength [32]. Additionally, the accuracy of hole fabrication, drilling, riveting technique, rivet shaping, and clamping force (which introduces residual stresses) all affect stress distribution [33]. Finally, operating conditions, such as the magnitude and direction of applied forces, as well as environmental conditions, significantly influence the distribution of contact stresses and, consequently, the strength and capacity of the riveted joints.

Riveted joints consist of two or more components connected by rivets that are deformed to ensure a durable connection and structural integrity. During assembly, contact between the rivet and hole generates stresses that affect the load capacity and fatigue strength of a joint [34]. Key stress zones include the rivet-hole interface (shear and normal stresses), the area under the rivet head (compressive stresses), and the rivet shank (circumferential stresses) [35]. Liu et al. [36] investigated the impact of forced installation caused by hole misalignment on the three-dimensional stress distribution and damage in a composite bolted joint. They proposed an analytical model of stresses distributed around composite holes and, using Hertz's theory, derived the maximum extrusion load through a deformation expression. The predicted stress distribution from the analytical model was compared with finite element (FE) simulation results that accounted for composite damage. The findings show that hole misalignment introduces a centrally symmetric stress distribution. As the misalignment increases, the composite strength decreases due to extrusion-induced damage. Existing analytical models, such as the classical Hertz contact theory, provide useful approximations for local stresses under idealized contact conditions but often fail to capture the complex, nonlinear interactions arising from real geometries and materials. On the other hand, FEM offer high fidelity but are computationally expensive and often not suitable for rapid engineering design. Modern contact stress analysis extends beyond classical Hertz theory, combining analytical, numerical, and experimental methods to address material nonlinearity and surface complexity. Applications range from astronaut training systems

[37], pneumatic actuator control [38], and piston synchronisation [39], to 3D roughness measurement [40], coating transparency tests [41], and studies on the aerodynamic effects of coating ageing in aerospace structures [42].

The aim of this experimental study was to determine the effect of the hole chamfer in a single-lap riveted joint on contact stresses. The analytical model is compared through finite element simulations and experimental tests performed on aluminium sheet specimens joined by blind rivets. The novelty of this study lies in introducing a geometric correction factor into the Hertz model and correlating it with physical hole chamfer size and angle. The combined experimental, numerical, and analytical results provide new insight into the local stress fields of riveted joints under different loading conditions.

ANALYTICAL MODEL OF CONTACT STRESSES

Classical Hertz contact theory

Accurate analytical modeling of contact stresses is essential for understanding the mechanical behavior of riveted joints under load. Classical contact theories, such as Hertz's solution [43, 44], provide closed-form expressions for estimating stresses and deformations in contact zones between elastic bodies. However, their assumptions - perfectly smooth surfaces, isotropic materials, no friction, and a relatively small contact area compared to the size of the bodies – limit their applicability to real-world engineering problems involving geometric complexity and material nonlinearity [45, 46]. Hertz's theory specifically addresses contact between curved elastic bodies, including sphere-to-flat, sphere-to-sphere, and cylinder-to-cylinder configurations [44]. It defines parameters such as contact area, pressure distribution, indentation depth, as well as contact force, based on material properties and body geometry [43]. The graphic definition is presented in Figure 1.

The most important values used in the calculations of stresses according to Hertz were:

- a relative diameter of curvature is defined as:

$$\frac{1}{d_*} = \frac{1}{d_1} + \frac{1}{d_2} \tag{1}$$

where: d_1 – the diameter ofz the female part (negative), d_2– the diameter of the male part (positive).

An equivalent module of elasticity for materials of cylinders is:

$$\frac{1}{E_*} = \frac{1-\nu_1^2}{E_1} + \frac{1-\nu_2^2}{E_2} \tag{2}$$

where: E_1 – Young's Modulus of the material of part 1, E_2 – Young's Modulus of the material of part 2, v_1 – the Poisson's ratio of the material of part 1, v_2 – the Poisson's ratio of the material of part 2.

The width of the contact surface for a cylinder-cylinder contact (the parameter b) is defined as:

$$b = \left(\frac{2F}{\pi L} \cdot \frac{d_*}{E_*}\right)^{1/2} \tag{3}$$

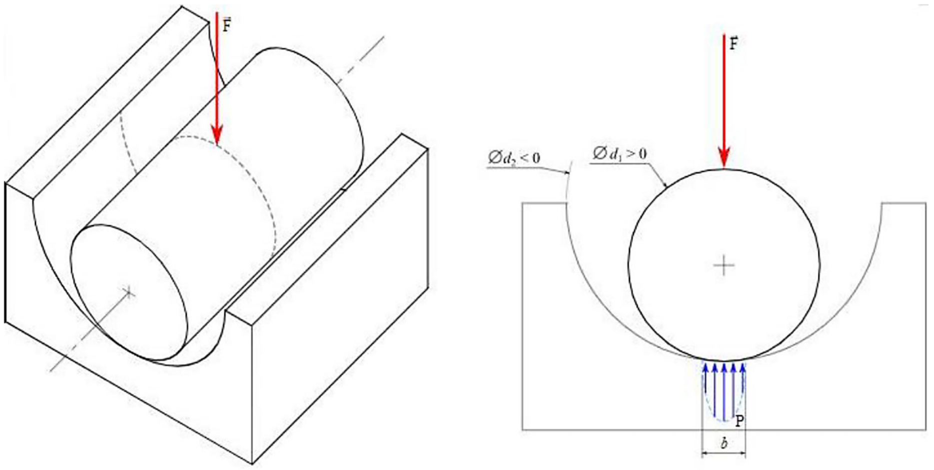

Figure 1. Geometric definition of the Hertz problem

The maximal stress located in the geometric center of contact is:

$$P_{max} = \frac{2F}{\pi b L} = \sqrt{\frac{2FE_*}{\pi L d_*}} \tag{4}$$

Modified Hertz model for rivet – hole interface

In this case of single-lap riveted joints with blind rivets with specific chamfering angles (e.g., 30°, 45°, 60°), the actual contact geometry significantly deviates from the classical scenarios described by Hertz. The contact area becomes a hybrid between cylindrical and conical contact, leading to increased local stress concentrations and a reduction in the effective contact length. Furthermore, the presence of friction, possible material plasticity, as well as the relationship between contact radius and chamfering geometry must be considered [20, 46].

For countersunk holes with a typical depth of approximately 0.5 mm and an angle of 45°, a correction factor of approximately $f_c \approx 1.3$ was used. As the chamfering angle increases, the contact tends to become more point-like, which intensifies the local stress concentration effects. To account for these geometric and physical differences, a modification to the classical Hertzian model was proposed, which includes:

Accounting for the actual contact area, given by the expression:

$$A_c = \pi d_c \cdot l_c + \pi r_c^2 \tag{5}$$

where: d_c – effective contact diameter (typically equal to the rivet diameter), l_c – cylindrical contact length after subtracting the chamfered region, r_c – effective contact radius corresponding to the chamfered (conical) zone.

The generalization of the contact stress equation was formulated as:

$$\sigma_{c,max} = \left(\frac{6F_n}{\pi b d}\right) \cdot f_c(\alpha) \tag{6}$$

where: F_n – normal force (rivet-to-hole clamping force), d – rivet diameter, $f_c(a)$ – chamfer angle correction factor, which accounts for the geometric and stress distribution effects specific to the presence of countersunk holes.

In this study, $f_c(a)$ was calibrated using results from finite element simulations. Three variants of chamfer size were modeled (0 mm, 0.1 mm, and 0.5 mm), and the resulting contact stress distributions were compared with those predicted by the classical Hertz model. A nonlinear least squares fitting procedure was applied to determine a correction function. For the tested range of chamfers, a value of $\alpha = 0.65$ yielded the best agreement with FEM results.

Results of the analytical analysis

For the analyzed riveted joint, the diameter dimensions were determined experimentally using an optical microscope. Next, by using the material properties listed in Table 2 and applying equations of the modified model Hertz, the stresses were calculated for different forces. To validate the obtained values, simple strength calculations typical for a riveted joint were conducted, as illustrated in Figure 2. These calculations assumed no clearance, considering only compressive stresses. The stresses were determined using Equation7. The computed stress results for the analyzed loading force values are summarized in Table 1.

$$P_{max*} = \frac{F}{d_1 L} \tag{7}$$

The analytical calculations determined the stress values (Hertzian and pressure) as a function of the applied force for the analyzed rivet joint. The analysis showed that increasing the size of the hole chamfer leads to a significant rise in the contact stress values. For all analyzed load magnitudes, a systematic increase in stress is observed both in the Hertz model and in the approach accounting for surface pressure without clearance. For example, for a load of F = 800 N, the Hertzian contact stress increases from 305.58 MPa (f = 0 mm) to 397.25 MPa (f = 0.5 mm), which represents an increase of over 30%.

At the same time, the comparison between the two approaches indicates that the stress values obtained from the Hertz model are significantly higher than those calculated from surface pressure. These differences are particularly evident in the absence of a chamfer or when the chamfer is small – for f = 0 mm, the Hertzian stresses are on average 36% higher than the contact stresses calculated assuming no clearance. This results from the fact that the Hertz model assumes a very small, point-like contact area, which leads to higher localized

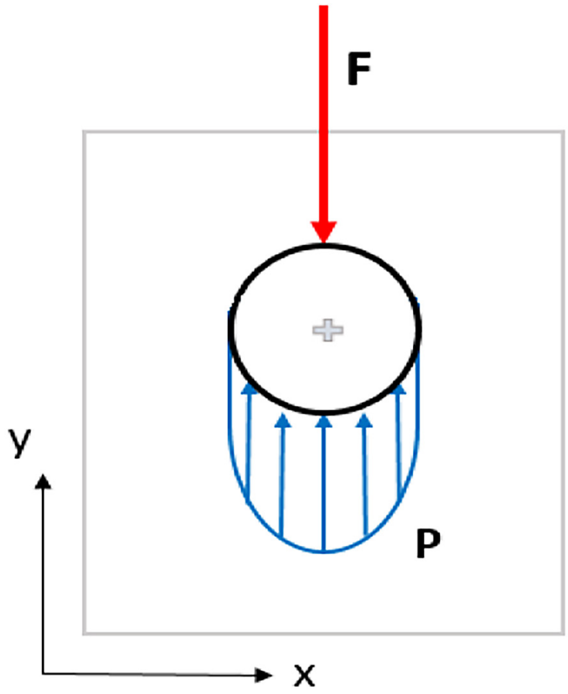

Figure 2. Stress between two objects in contact (without clearance)

stresses. In contrast, the pressure stress (no clearance) approach reflects a more realistic distribution of force over a larger contact surface, accounting for effects such as plasticity. As the chamfer radius increases, this difference gradually decreases, reaching only about 1.5% for f = 0.5 mm. This suggests that with a sufficiently large chamfer, the contact area becomes geometrically constrained by the chamfer itself, reducing the effect of extreme stress concentrations. For large chamfers, the results for both models showed that the dominant factor influencing contact stress values becomes the geometric limitation of the contact surface.

The described and analyzed values of Hertzian contact stress and pressure stress are presented on the graphical plots below (Figure 3, Figure 4). The curves with marked values clearly illustrate the influence of the hole chamfer on stress with different load values.

EXPERIMENTAL STUDIES ON RIVET JOINTS WITH A BLIND RIVET

The geometry of joints and materials

In the presented work, a single-lap joint with blind rivets was examined. The geometry of the riveted joint is illustrated in Figures 3 and 4. The dimensions of the joint were taken from ISO 12996 [47]. The sheets were made of EN AW 2017A aluminum alloy with a thickness of 1 mm, and the blind rivets were made of EN AW 5251 aluminum alloy with a diameter of 4 mm. According to the standard [47], to ensure the axial nature of the load, additional plates should be glued to the ends of the joined sheets (Figure 5). The mechanical properties of the sheet and blind rivet materials are presented in Table 2.

Results of the experimental analysis

The static strength tests of lap joints were conducted by ISO 12996 guidelines (Figure 6). The shear tests were performed using a Zwick-Roell tension machine equipped with an extensometer and a force transducer with a nominal force value of 50 kN. The static tests were carried out at a traverse speed of 4 mm/min, allowing for the creation of a shear diagram for the investigated riveted joint.

During the joint shear test, the actual force F (with a measurement accuracy of 0.12% of the nominal force value) and the sheet displacement s (measurement uncertainty 0.5 µm) were monitored and recorded. For each hole chamfer size, 15 samples were made. The following designations were adopted for the respective geometric configurations of the samples: A0 for f = 0 mm, A01 for f = 0.1 mm, and A05 for f = 0.5 mm. All results of the tests and series were summarized on the graphs. Subsequently, the experimental results were statistically analyzed, and representative curves were selected for further analysis. The results were illustrated in Figure 7.

Table 1. Results of analytical analysis of contact stress

Force F [N]	f = 0 mm		f = 0.1 mm		f = 0.5 mm	
	Hertz contact stress [MPa]	Pressure stress (no clearance) [MPa]	Hertz contact stress [MPa]	Pressure stress (no clearance) [MPa]	Hertz contact stress [MPa]	Pressure stress (no clearance) [MPa]
200	76.39	48.8	84.03	54.3	99.31	97.8
600	229.18	146.6	252.1	162.9	297.94	293.4
800	305.58	195.5	336.14	217.3	397.25	391.2

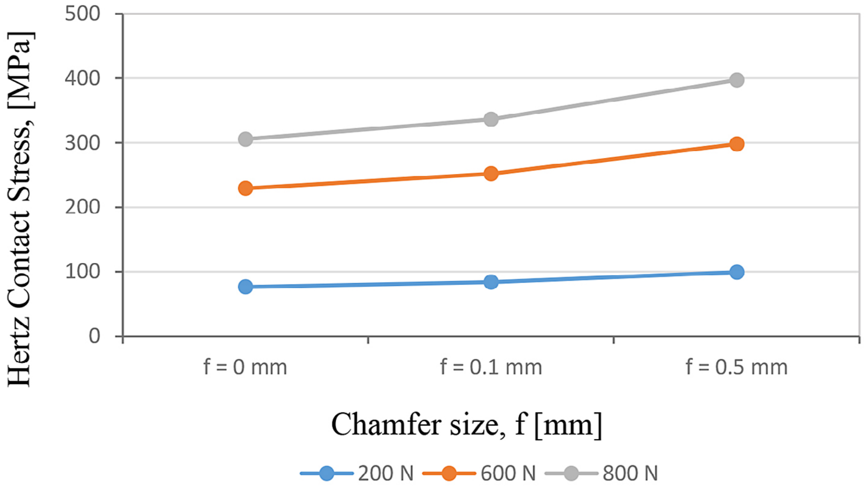

Figure 3. Hertz contact stress of riveted joints for different chamfer sizes and loads

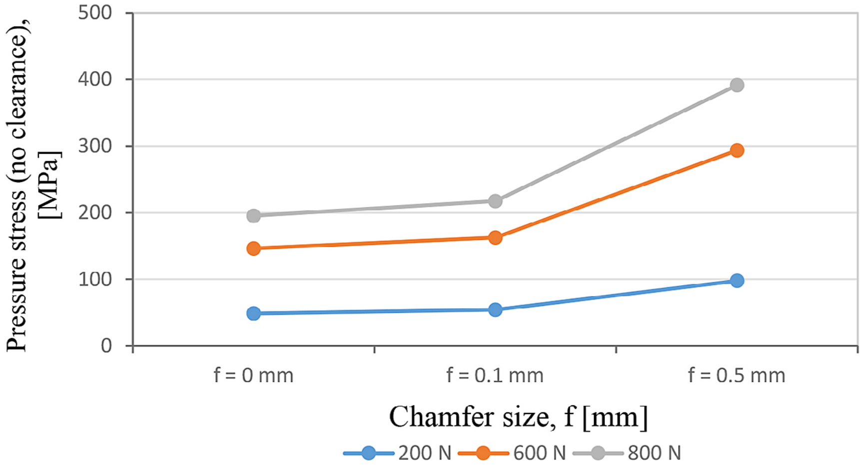

Figure 4. Pressure stress (no clearance) of riveted joints for different chamfer sizes and loads

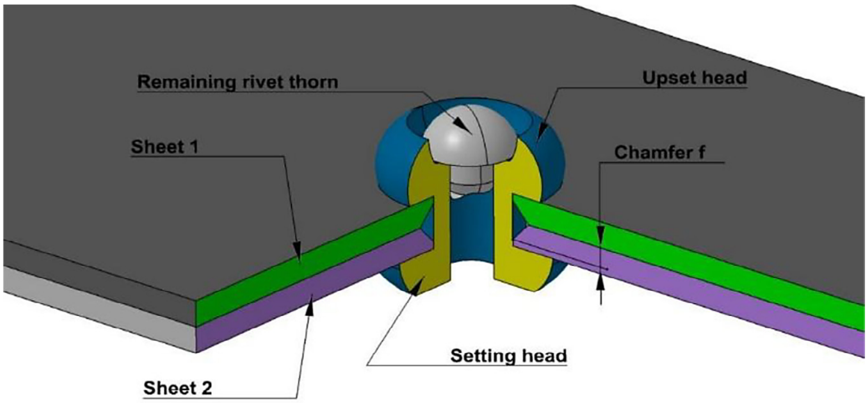

Figure 5. Geometry of joint [48]

All curves show nonlinear behavior, with a distinct peak followed by a force drop, indicating permanent plastic deformation and failure of the riveted joints. The displacement at maximum force and the force magnitude differ for each curve, showing differences in the failure behavior. As it can be seen from this graph, for the joint with f = 0 mm (A0), the maximum force is

Table 2. Mechanical properties of the materials examined [49]

Aluminum alloy	Young modulus E [GPa]	Poisson's ratio	Yield stress $Rp_{0.2}$ [MPa]	Ultimate tensile strength UTS [MPa]
EN AW 2017 A	72	0.3	140	210
EN AW 5251	68	0.3	110	200

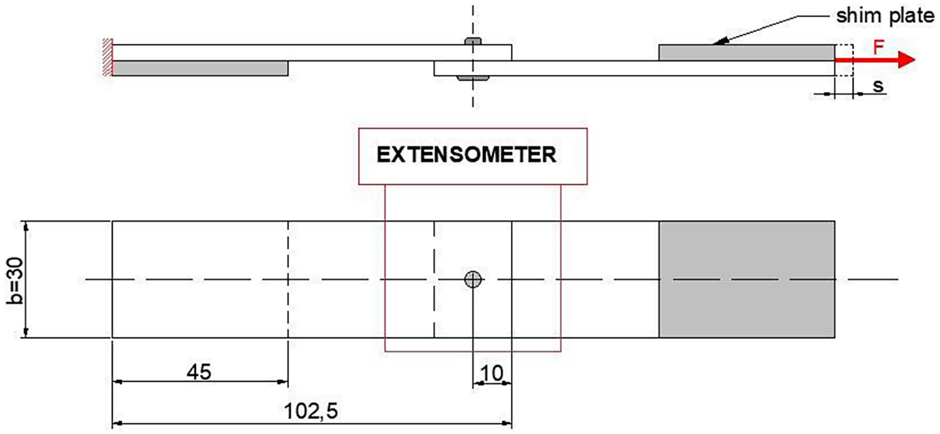

Figure 6. Geometry, load, and boundary conditions of joints used in experimental analysis

955 N and the displacement s = 1.63 mm before failure. The curve declines sharply after reaching the maximum capacity, indicating the shear of the rivet. The results for A01 showed that the maximum force was at the higher displacement (s = 2 mm). The decline after the peak is more gradual than A0, suggesting better plastic deformation capacity. The shear curve for A05 showed the highest maximum force (F = 1191 N) and demonstrated the largest displacement s = 2.5 mm before failure. The curve showed a gradual increase and a smoother decline, indicating a complex stress state. Initially, bending occurred, followed by shear of the riveted joint. The results of experiments showed that the capacity and the displacement depend on the chamfer size.

Due to the limited number of specimens tested for each geometric configuration, the measurement uncertainty was estimated using the Student's t-distribution [50]. The standard deviation S of the mean value obtained from the experiments was calculated based on the following formula:

$$S = \sqrt{\frac{\sum_{i=1}^{n}(x_i - x)^2}{n(n-1)}} \tag{8}$$

where: n – number of samples, x_i – value obtained in the i-th sample, x – arithmetic mean of the values obtained in n samples.

For joints with f = 0.5 mm configuration, the standard deviation was 55.94 and for riveted joints without chamfer (f = 0 mm) was 38.28. The standard deviation was small, indicating the repeatability of the results and the stable behavior of the riveted joints in the experimental tests.

Additionally, the cross-sections of riveted joints were prepared. For all geometrical configurations, the shear process of the rivet was interrupted at different stages of loading. Next, the joints were covered by the epoxy resin. After the hardening of the resin, the joints were cut and polished. The prepared cross-sections from the experimental analysis and photos from the microscope allowed for the visualization of the deformation state of the riveted joint. The author's technology of making riveted joint cross-sections was developed during a static tensile test [51]. Figure 8 (for joint without chamfer f = 0 mm) and Figure 9 (for joint with f = 0.5 mm) show shear curves with cross-sections of the riveted joint at the chosen and critical points of the shear process. In both cases, small deformations of the rivet and hole were observed at low loads. When the applied force approached its maximum value (for f = 0 mm, in case F = 900 N, Figure 8), visible deformation of the rivet occurred, primarily due to the shear process. The initially smooth internal cylindrical surface of the rivet became distorted and displaced as a result of localized high shear

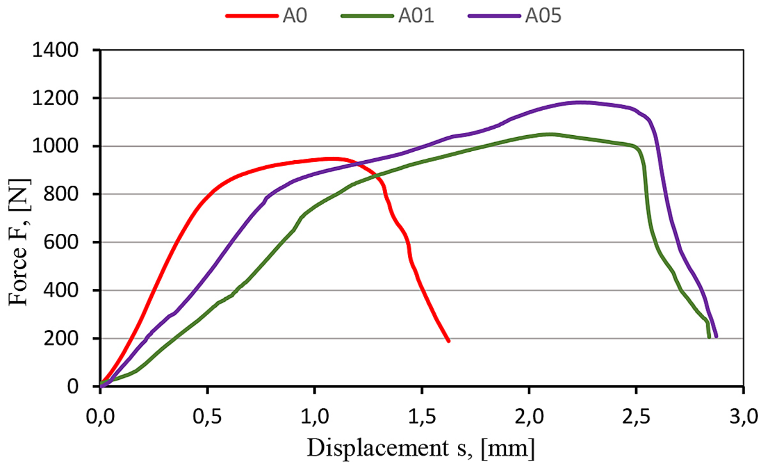

Figure 7. Shear curves for single-lap riveted joints with different sizes of hole chamfer

stresses. Additionally, at the advanced stage of loading, a gap between the joined materials was observed (Figure 9). In contrast, a markedly different rivet deformation pattern was observed in specimen A05 (with a chamfer f = 0.5 mm) (Figure 9). At a high load of F = 1100 N, the rivet underwent significant bending deformation. Notably, no internal shift of the cylindrical surface is detected in this case.

NUMERICAL ANALYSIS

Discrete model

Numerical analysis of single-lap riveted joints with blind rivet configurations was conducted using 3D finite element models developed and evaluated with the commercial finite element software ANSYS. The geometric model employed in the numerical study corresponded to the riveted joints used in the experimental work (Figure 3).

Elasto-plastic material models were analyzed, with the true stress-strain curves for the bilinear material model of the sheet and blind rivet depicted in Figure 10. The material properties used to define these models are summarized in Table 3.

The numerical analysis was based on assumptions reflecting loading conditions from earlier experimental tests. Accurately modelling the axial load from the static tensile test was essential to ensure consistency between experimental and numerical results. The following FEM boundary conditions were applied: the right end of the sheet and the right additional surface were constrained (fixed support - all degrees of

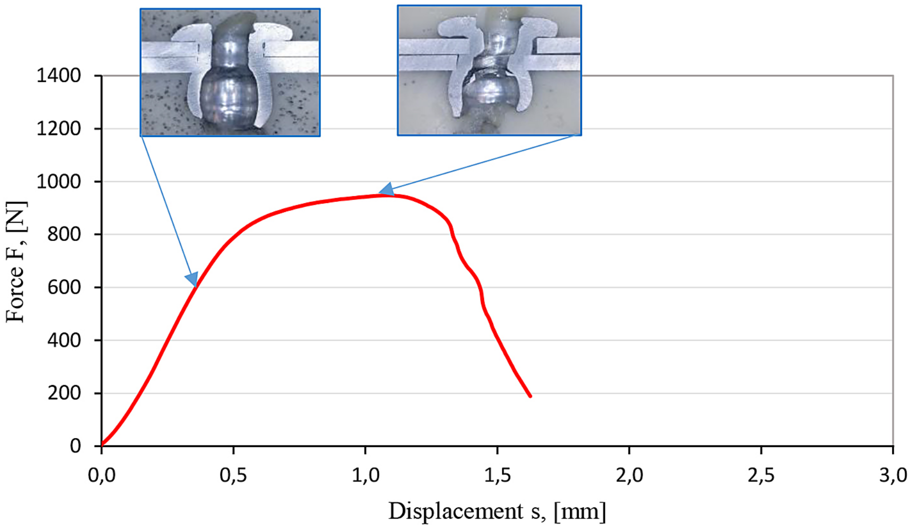

Figure 8. Shear curve for a riveted joint with chamfer f = 0 mm

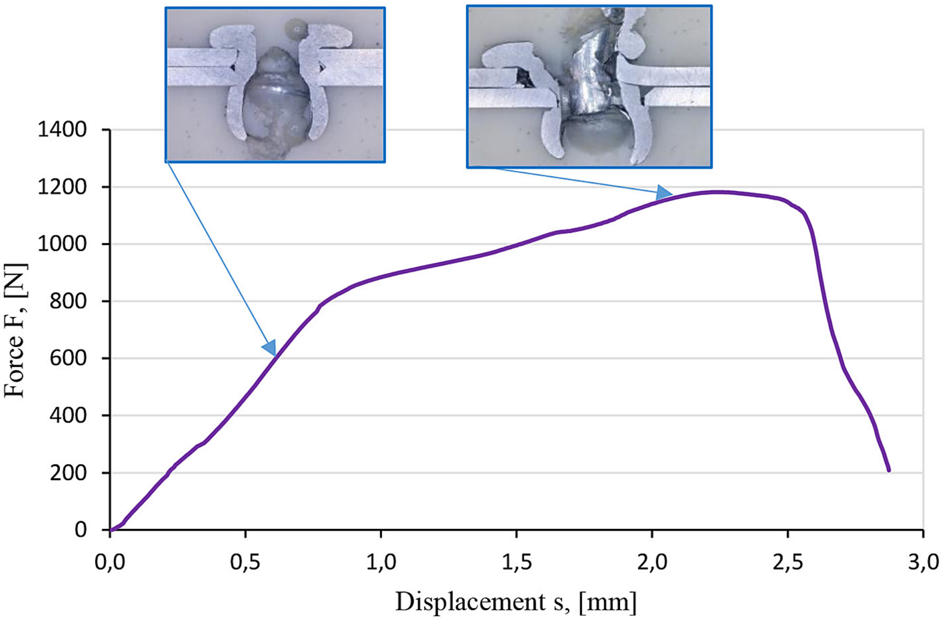

Figure 9. Shear curve for a riveted joint with chamfer f = 0.5 mm

freedom were fixed); the left end of the sheet and the left additional surface allowed displacement in the x-direction (free), while displacements in the y and z directions were constrained to 0. An external force F [N] was applied in the x-direction at the left end. Contact models were selected based on the simulations replicating the joint's working conditions and aligned with prior studies. Defined contacts included sheet-to-sheet and hole-to-rivet frictional interfaces, both with a coefficient of 0.2. The FE model comprised three bodies (rivet and two sheets, Figure 11), meshed with over 900,000 10-node tetrahedral elements. A simplified rivet model (Figure 11a), previously used in riveting process simulations, was adopted. Mesh size and density were refined through convergence studies.

Results of the numerical analysis

As part of the numerical analysis of a rivet connection subjected to axial tension, several loading forces were selected for the analysis. The maximum load capacity of the tested joint was 955 N for A0. Therefore, the tests considered forces of 200 N, 600 N, and 800 N, which represent approximately 80-90% of the total strength of the joint, just before the failure of the riveted joint. To provide a clearer explanation of the size chamfer effect and its impact on the deformation behavior, the publication discusses the stress distributions for all chamfer sizes for 800 N.

The results were illustrated in Figure 12. For f = 0 mm, the lowest maximum equivalent stress value was observed among all analyzed configurations. The maximum stress was 244.02 MPa occurred at the edge region of the sheet in contact with the rivet shank, where a pronounced stress concentration was identified (Figure 12a). The absence of a chamfer leads to a strong localised stress at the contact interface. For the configuration with a chamfer f = 0.1 mm (Figure 12b), the maximum equivalent stress increased to 669.52 MPa. The stress distribution was more symmetrical and dispersed around the rivet shank, with concentrations evident in the lateral and lower regions of the sheet. The highest maximum stress value was noted for the configuration with f = 0.5 mm - 748.65 MPa (Figure 12c). The widespread zone of elevated stress, extending across both the upper and lower sheets and over a substantial area of the rivet, was observed. The observed stress field indicates a strong interaction at the contact interface, which implies enhanced utilization of the material and joint load capacities.

Figure 13 shows the contact pressure for riveted joints. When analyzing the load case with a force of 800, the lowest contact pressure was observed for the configuration without a chamfer (Figure 13a), with a value of 187.03 MPa. In this case, no significant stress concentrations were identified, and the pressure distribution remained uniform, primarily along the lateral surfaces of the hole. An increase in chamfer

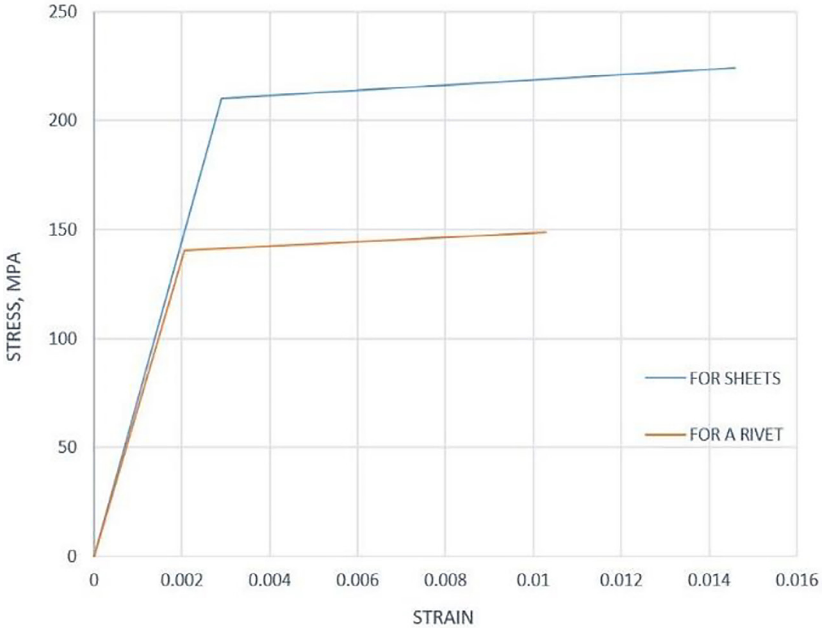

Figure 10. Stress-strain curve of the bilinear material model for sheets and a rivet [6]

Table 3. Material properties of the bilinear material model

Material data	Aluminum alloy EN AW 2017A (sheet)	Aluminium alloy EN AW 5251 (rivet)
Density [kg/mm^3]	2700	2700
Young's modulus [GPa]	72	68
Poisson's ratio	0.3	0.3
Yield strength [MPa]	210	140
Tangent modulus [MPa]	1200	1000

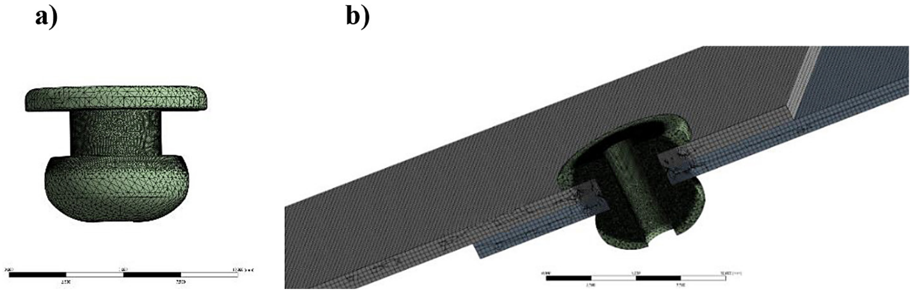

Figure 11. Mesh: a) rivet; b) riveted joint (cross-section)

depth led to a considerable rise in the maximum contact pressures within the single riveted joint, from 443.27 MPa (Fig. 13b) for f = 0.1 mm to 613.09 MPa for f = 0.5 mm (Figure 13c). Additionally, the pressure distribution is sharper near the central contact area. For higher chamfer sizes observed the pressure gradient is steep, showing that most of the load is concentrated in a smaller area, which may lead to higher localized deformation or potential wear.

COMPARISON OF RESULTS

To compare the experimental and numerical deformation results, extreme cases of the joint configuration are presented in Figures 14 and 15.

For the results for the joint without chamfer (f = 0 mm) and with F = 800 N (Figure 14), a strong correlation with the numerical model was observed. The experimental cross-section revealed separation of the sheets, deformation of

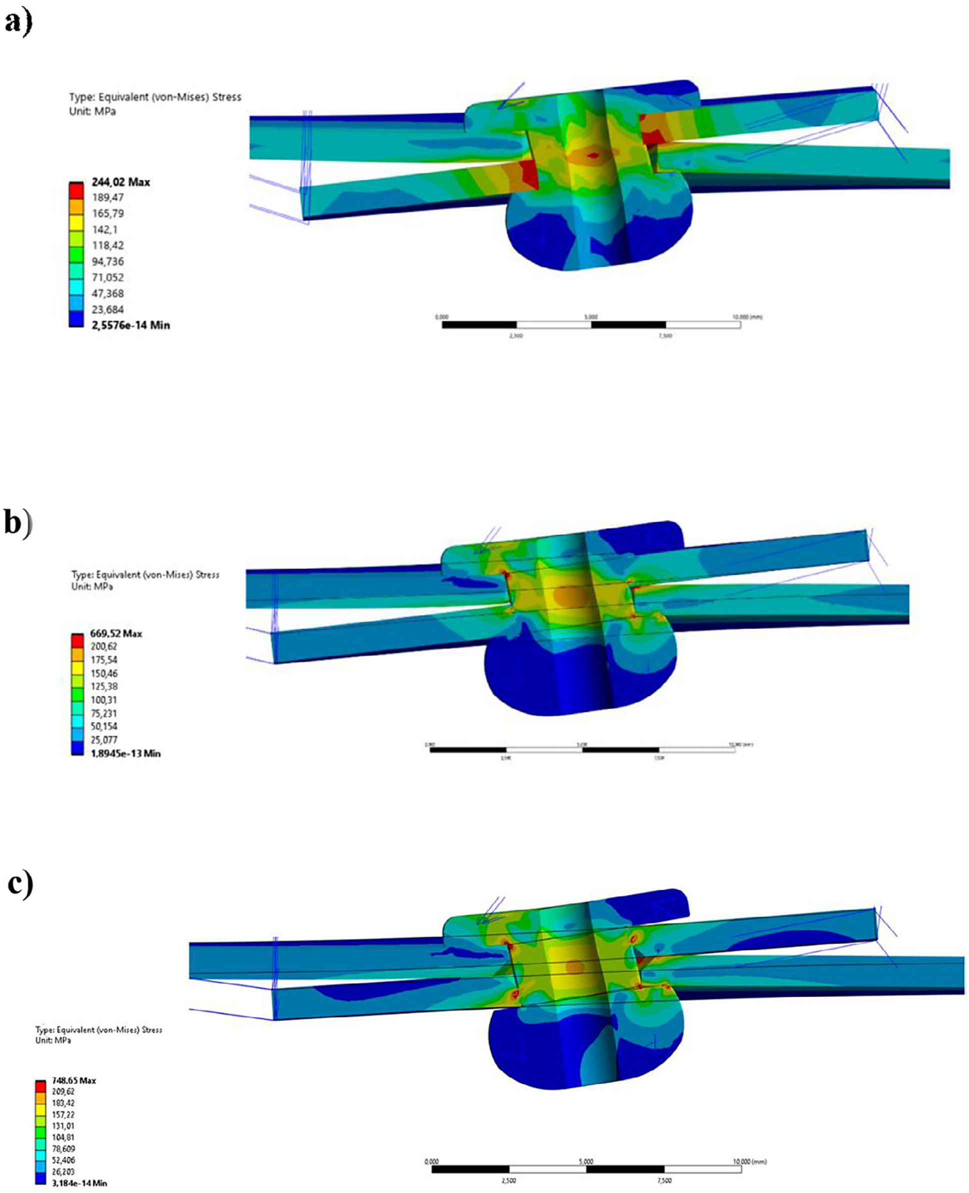

Figure 12. The equivalent stress of the single-lap riveted joint for F = 800 N: a) f = 0 mm, b) f = 0.1 mm, c) f = 0.5 mm

the rivet head, and a characteristic outward extrusion of the rivet pin (Figure 14a). The numerical analysis indicated considerable displacement of the upper sheet and rotation of the rivet shank (Figure 14b). In both cases, notable similarity was observed in the actual displacement distribution, deformation of the rivet shank and sleeve, and the response of sheets to increasing load. The riveted joint with a chamfer of f = 0.5 mm exhibited the greatest deformations compared to smaller chamfers (f = 0.1 mm) (Figure 15). Even under moderate loading conditions (F = 800 N), a noticeable loss of symmetry was observed, and at maximum load, significant displacement and damage to the rivet occurred. The FEM models accurately replicated the deformation behavior, particularly in the hole and sheet regions. While the use of a larger chamfer improves rivet forming efficiency, it simultaneously increases the risk of local overloading.

Table 4 presents the experimental and numerical values of the total deformations for the applied loads. For the numerical models, the total deformation maximum was higher by an average of 19% (for F = 200 N and f = 0 mm) than the experimental results of deformations. For higher loads (600–800 N), the numerical model showed good agreement with experimental data, especially for chamfer sizes 0.1 mm and 0.5 mm, where errors remained mostly below 10%.

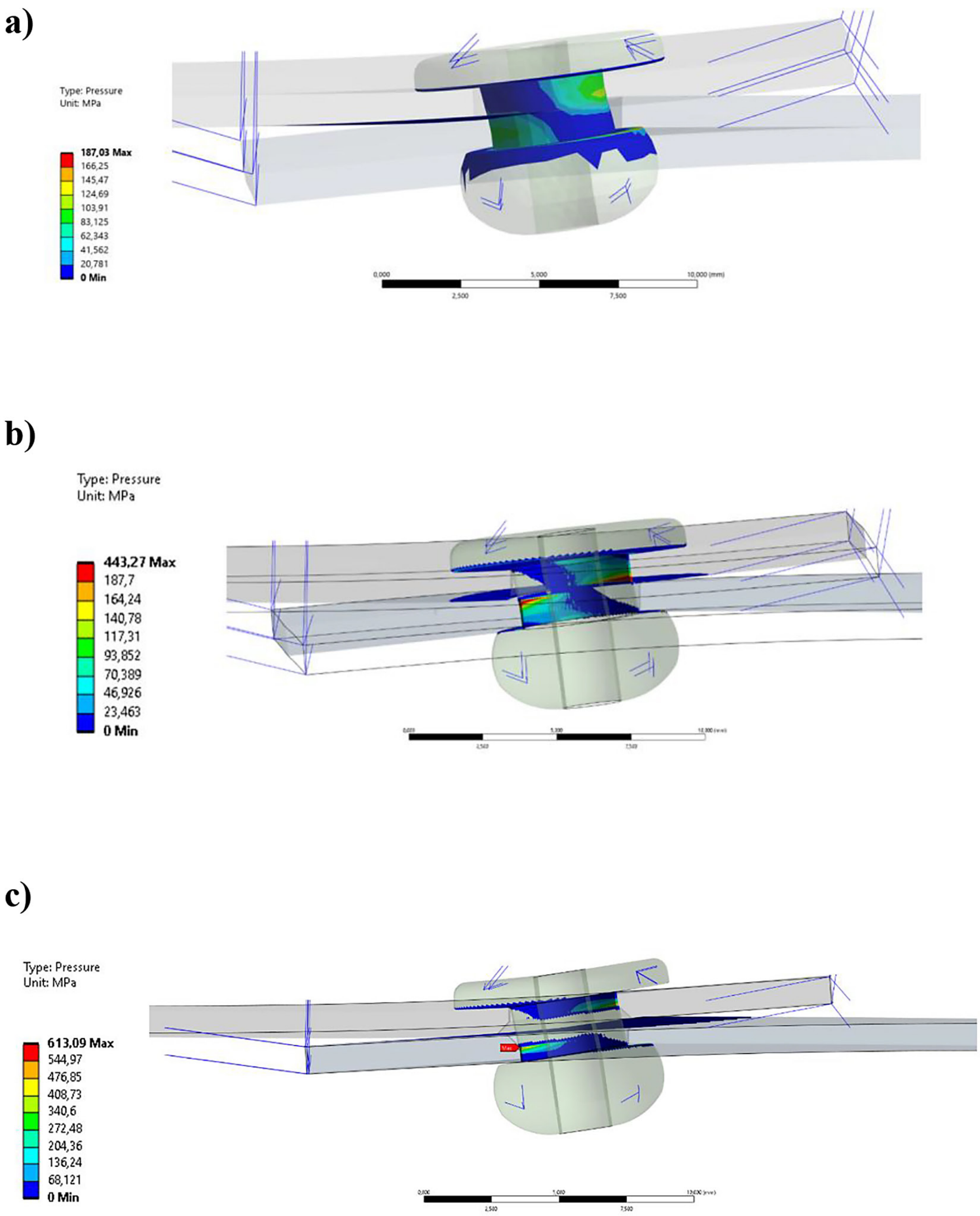

Figure 13. Contact pressure for F = 800 N: a) f = 0 mm, b) f = 0.1 mm, c) f = 0.5 mm

In order to compare the obtained analytical and numerical contact stress results for all considered configurations are presented in Table 5. A comparison between the numerical and analytical contact stress results (with percentage error between Hertz and numerical) for different hole chamfer configurations revealed clear trends in model agreement. The maximum contact pressures obtained numerically (Contact Pressure Max) were consistently higher than those calculated analytically using Hertzian theory and pressure stress without clearance. However, the degree of this discrepancy varied depending on the chamfer size and load level. In the configuration with f = 0 mm, the differences between the numerical and analytical results were relatively moderate. The maximum contact pressure in this case was only about -8% lower than the pressure stress and -39% lower than the Hertzian estimate, suggesting that the simplified analytical models approximate the stress behavior reasonably well for geometries without a chamfer. In contrast, for f = 0.1 mm, the numerical model showed significantly higher values. At 800 N,

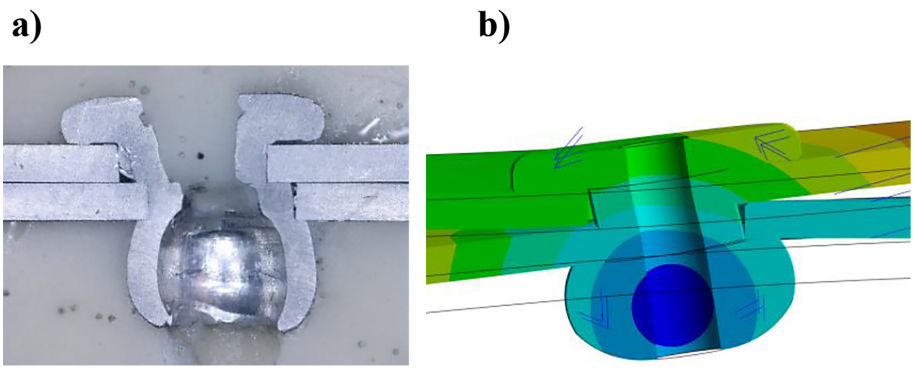

Figure 14. Cross-section of the riveted joint with f = 0 mm and load F = 800 N from: a) experiment, b) numerical analysis

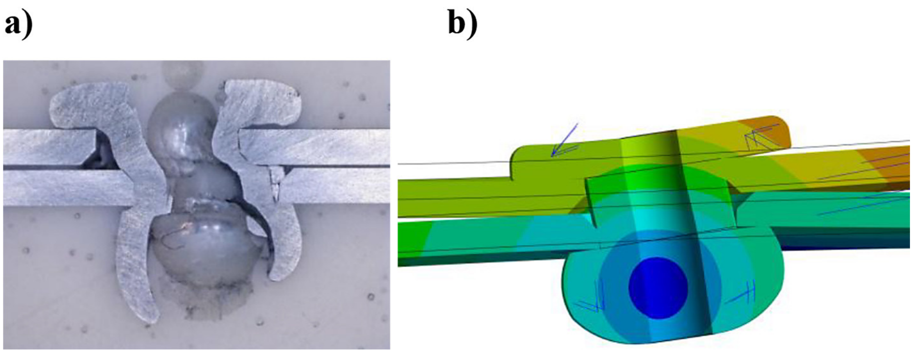

Figure 15. Cross-section of the riveted joint with f = 0.5 mm and load F = 800 N from: a) experiment, b) numerical analysi

Contact Pressure Max reaches 443.27 MPa – approximately +104% higher than pressure stress and +32% higher than Hertz stress. The largest differences were noted for f = 0.5 mm. Here, the numerical contact stress exceeds both analytical estimates by a large margin. These represent increases of over +137% and +140%, respectively. This suggests that the numerical model captures significant nonlinearities and localized effects – such as stress triaxiality and asymmetric deformation - which analytical methods tend to overlook.

The described, compiled, and compared values of analytical contact stress and numerical contact pressure are presented graphically in the charts below (Figures 16–18). The curves with marked values clearly illustrate the trends and

Table 4. Comparison of the elongations of the riveted joint obtained numerically and experimentally, for different force values, with the percentage error to the experimental value

Chamfer size f [mm]	Force F [N]	Experiment [mm]	Numerical analysis [mm]	Numerical analysis [%]
		Total deformation maximum		
0	200	0.1443	0.1722	19.33
	600	0.3517	0.3915	11.32
	800	0.5103	0.4862	4.7
0.1	200	0.3449	0.3912	13.42
	600	0.8348	0.912	9.3
	800	1.1149	1.1762	5.5
0.5	200	0.2050	0.2299	12.14
	600	0.6087	0.7101	16.7
	800	0.7938	0.8528	7.43

Table 5. Comparison of contact stress of the riveted joint obtained numerically and analytically, for different force values and three configurations of hole chamfer size, with percentage error

Force F [N]	f = 0 mm				f = 0.1 mm				f = 0.5 mm			
	Hertz contact stress [MPa]	Pressure stress (no clearance) [MPa]	Contact pressure max [MPa]	Δ Hertz vs Num. [%]	Hertz contact stress [MPa]	Pressure stress (no clearance) [MPa]	Contact pressure max [MPa]	Δ Hertz vs Num. [%]	Hertz contact stress [MPa]	Pressure stress (no clearance) [MPa]	Contact pressure max [MPa]	Δ Hertz vs Num. [%]
200	76.39	48.8	42	81	84.03	54.3	108.51	22	99.31	97.8	234.98	57
600	229.18	146.6	107.43	113	252.1	162.9	326.13	22	297.94	293.4	407.32	26
800	305.58	195.5	187.03	63	336.14	217.3	443.27	24	397.25	391.2	613.09	35

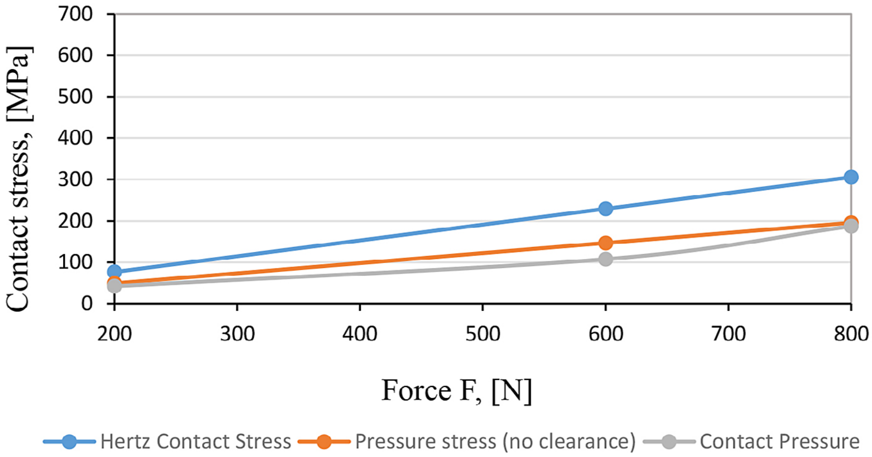

Figure 16. Comparison of contact stress for f = 0 mm for the examined loads

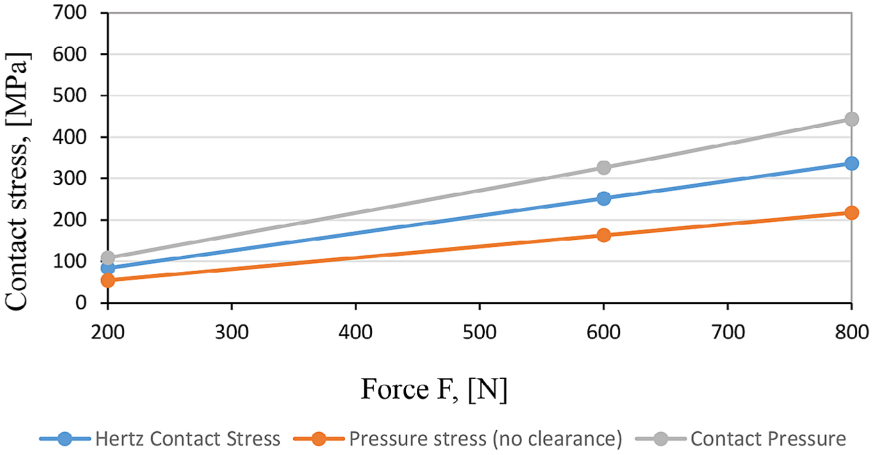

Figure 17. Comparison of contact stress for f = 0.1 mm for the examined loads

changes in stress values for a given geometric configuration of the riveted joint sample.

CONCLUSIONS

The main goal of this study was to conduct an analysis of the influence of the hole chamfer size of a single lap joint with a blind rivet on the deformation and contact stresses. In this work, experimental results of blind rivet joints were presented. Contact stresses and stress distribution in the riveted joint cross-section were analyzed. The results of the experimental analysis were not only compared with numerical results, but also using the modified Hertz stress mathematical model.

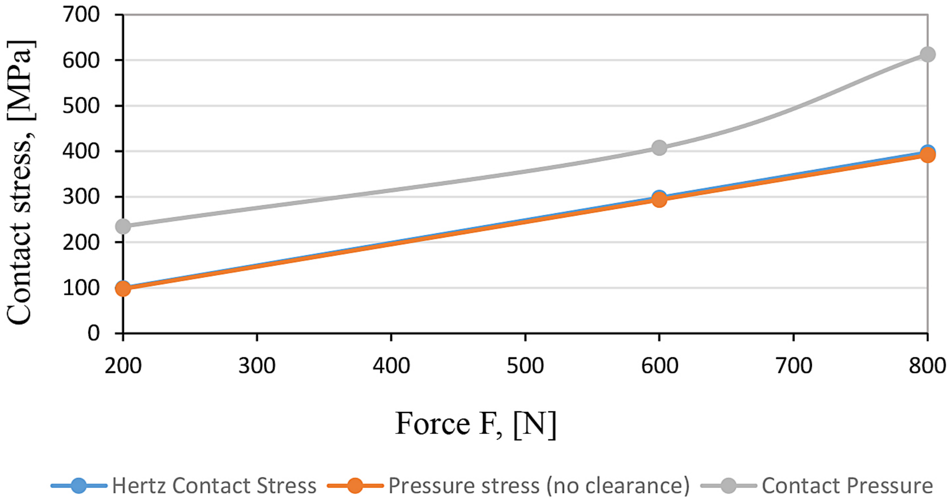

Figure 18. Comparison of contact stress for f = 0.5 mm for the examined loads

The results obtained from these investigations led to the following conclusions:

1. The size of the hole chamfer has a significant impact on both the magnitude and distribution of contact stresses in riveted joints.
2. The highest maximum equivalent stress was observed for joints with a chamfer size of f = 0.5 mm, reaching up to 748.65 MPa. This configuration also exhibited the most extensive plastic deformation, especially in the rivet shank and sheet regions.
3. Experimental cross-section analysis confirmed that larger chamfer sizes promote more symmetrical deformation and improve rivet forming.
4. For joints without chamfer (f = 0 mm), the maximum contact pressure was lowest and stress distribution was more uniform, but the strength capacity was significantly reduced compared to chamfered configurations.
5. The modified Hertz model incorporating chamfer geometry showed better correlation with numerical results for smaller chamfers, reducing the error margin between analytical and FEM results to less than 2%.
6. Comparative analysis between experimental and numerical results showed strong qualitative agreement in deformation and stress distribution, validating the robustness of the combined methodology used.
7. The study provides a comprehensive methodology for evaluating riveted joint performance under axial loads, offering insights for improved joint design in aerospace and structural applications.

Acknowledgment

The research presented in this work was supported by Department of Aerospace Engineering, Faculty of Mechanical Engineering and Aeronautics, Rzeszow University of Technology (Project no. DS.ML.25.001)

REFERENCES

1. Johnson KL, Johnson KL. Contact mechanics. 5.Reprint. Cambridge: Cambridge Univ. Press; 1999. 452. http://dx.doi.org/10.1177/0954406216634121
2. Ghaednia H, Jackson R, Lee H, Rostami A, Wang X. Contact mechanics. In: Tribology for Scientists and Engineers: From Basics to Advanced Concepts. 2013. 93–140. http://dx.doi.org/10.1007/978-1-4614-1945-7_3
3. Zheng M, Li Y, Wang C, Bai J, Wang L, Liu Z, et al. Prediction of contact stress in bolted joints using the Polynomial Chaos-Kriging model. Eng Fail Anal. 2023 Dec; 154: 107646. http://dx.doi.org/10.1016/j.triboint.2018.05.044
4. Glocker C. Formulation of spatial contact situations in rigid multibody systems. Comput Methods Appl Mech Engrg. 1999; https://doi.org/10.1016/S0045-7825(98)00381-8
5. Paszeczko M, Holubets V, Dziedzic K, Barszcz M, Montusiewicz J. Tribotechnika. Triboprocesy, materiały, technologie, optymalizacja. Lublin: Wydawnictwo Politechniki Lubelskiej; 2020.
6. Lubas M, Bednarz A. Material model effect for simulating a single-lap joint with a blind rivet. Materials. 2021 Nov 26; 14(23): 7236. https://doi.org/10.3390/ma14237236

7. Poon B, Rittel D, Ravichandran G. An analysis of nanoindentation in linearly elastic solids. Int J Solids Struct. 2008 Dec; 45(24): 6018–33. https://doi.org/10.1016/j.ijsolstr.2008.07.021
8. Mazurkow A. Calculation method for the distribution of normal stress in the contact area between a journal and a bushings bearing. Mechanik. 2015 Dec; (12): 975/133-975/138.
9. Chang Y, Ding J, Fan H, Ding Y, Lu H, Chen Y, et al. A hybrid method for bolted joint modeling considering multi-scale contact mechanics. Precis Eng. 2022 Nov; 78: 171–88. http://dx.doi.org/10.1016/j.precisioneng.2022.08.001
10. Alves J, Peixinho N, Da Silva MT, Flores P, Lankarani HM. A comparative study of the viscoelastic constitutive models for frictionless contact interfaces in solids. Mech Mach Theory. 2015 Mar; 85: 172–88.
11. Pinto-Borges H, Pinto J, Carvalho O, Henriques B, Silva F, Gomes J, et al. Stresses, friction, and wear on different materials and design for temporomandibular joint total joint replacement (TMJ TJR). Tribol Int. 2023 Feb; 178: 108051.
12. Dick T, Paulin C, Cailletaud G, Fouvry S. Experimental and numerical analysis of local and global plastic behaviour in fretting wear. Tribol Int. 2006 Oct; 39(10): 1036–44.
13. Komvopoulos K, Gong ZQ. Stress analysis of a layered elastic solid in contact with a rough surface exhibiting fractal behavior. Int J Solids Struct. 2007 Apr; 44(7–8): 2109–29. http://dx.doi.org/10.1016/j.ijsolstr.2006.06.043
14. Wang R, Zhu L, Zhu C. Research on fractal model of normal contact stiffness for mechanical joint considering asperity interaction. Int J Mech Sci. 2017 Dec; 134: 357–69.
15. Liao Y, Zhou Y, Huang Y, Jiang L. Measuring elastic–plastic properties of thin films on elastic–plastic substrates by sharp indentation. Mech Mater. 2009 Mar; 41(3): 308–18. doi:10.1016/j.actamat.2007.07.045
16. Palade AC, Pillon GP, Cicala E, Grevey D, Marsavina L. Subsurface treatment of a contact subjected to a hertz pressure. Int J Mech Sci. 2013 Dec 1; 77: 107–12.
17. Flores P, Machado M, Silva MT, Martins JM. On the continuous contact force models for soft materials in multibody dynamics. Multibody Syst Dyn. 2011 Mar; 25(3): 357–75. http://dx.doi.org/10.1007/s11044-010-9237-4
18. Jin M, Luo Y, Xu X, Xie B, Wang W, Li Z, et al. Normal contact stress analysis of large-deflection compliant mechanisms using a CPRBM-based method. Mech Mach Theory. 2024 Jan 1; 191: 105524. http://dx.doi.org/10.1016/j.mechmachtheory.2023.105524
19. Budynas RG, Nisbett JK. Shigley's mechanical engineering design. 9. ed. New York, NY: McGraw-Hill; 2011; 1082. (McGraw-Hill series in mechanical engineering).
20. Guo Z, Hao M, Jiang L, Li D, Chen Y, Dong L. A modified Hertz model for finite spherical indentation inspired by numerical simulations. Eur J Mech - ASolids. 2020 Sep; 83: 104042. http://dx.doi.org/10.1016/j.euromechsol.2020.104042
21. Skrinjar L, Slavič J, Boltežar M. A review of continuous contact-force models in multibody dynamics. Int J Mech Sci. 2018 Sep; 145: 171–87. http://dx.doi.org/10.1016/j.ijmecsci.2018.07.010
22. Askari E. Mathematical models for characterizing non-Hertzian contacts. Appl Math Model. 2021 Feb; 90: 432–47.
23. Wang G, Liu C. Further investigation on improved viscoelastic contact force model extended based on hertz's law in multibody system. Mech Mach Theory. 2020 Nov; 153: 103986. https://doi.org/10.1016/j.mechmachtheory.2020.103986
24. Merah A, Houari A, Madani K, Belhouari M, Amroune S, Chellil A, et al. Experimental Investigation Into the Tensile Strength Post-Repair on Damaged Aluminium 2024 -T3 Plates Using Hybrid Bonding/Riveting. Acta Mech Autom. 2024 Aug 1; 18(3): 514–25.
25. Mohd Tobi AL, Ding J, Bandak G, Leen SB, Shipway PH. A study on the interaction between fretting wear and cyclic plasticity for Ti–6Al–4V. Wear. 2009 Jun; 267(1–4): 270–82. http://dx.doi.org/10.1016/j.wear.2008.12.039
26. Shi W, Zhang Z. An improved contact parameter model with elastoplastic behavior for bolted joint interfaces. Compos Struct. 2022 Nov; 300: 116178. https://doi.org/10.1016/j.compstruct.2022.116178
27. Yan W, Sun Q, Feng XQ, Qian L. Analysis of spherical indentation of superelastic shape memory alloys. Int J Solids Struct. 2007 Jan; 44(1): 1–17. https://doi.org/10.1016/j.ijsolstr.2006.04.007
28. Hou P, Zhang W. Bolt coupling structure of contact stress and the influence factors of joint stiffness based on finite element Method. Procedia Comput Sci. 2022; 208: 658–65. http://dx.doi.org/10.1016/j.procs.2022.10.090
29. Wang L, Wang Y, Sun XG, Pan ZY, He JQ, Li CG. Influence of pores on the surface microcompression mechanical response of thermal barrier coatings fabricated by atmospheric plasma spray—Finite element simulation. Appl Surf Sci. 2011 Jan; 257(6): 2238–49. https://doi.org/10.1016/j.apsusc.2010.09.081
30. Derewońko A, Szymczyk E, Jachimowicz J. Numeryczne modelowanie zagadnienia kontaktu w procesie spęczania nitu. Biuletyn WAT 2006; VOL. LV, Nr 4.

31. Szymczyk E, Jachimowicz J. Analiza powierzchni kontaktu w połączeniu nitowym. Biuletyn WAT 2007; VOL. LVI, Nr 4.
32. Szymczyk E, Sławiński G. Numerical analysis of the riveted specimen. J KONES. 2007;Vol. 14, No. 2:475–84. https://doi.org/10.2478/v10164-012-0062-5
33. Shi W, Zhang Z. Contact characteristic parameters modeling for the assembled structure with bolted joints. Tribol Int. 2022 Jan; 165: 107272. https://doi.org/10.1016/j.triboint.2021.107272
34. Kudryavtsev AA. Plastic deformations under initial conditions of contact problem of mechanics (case study of riveted joints). Proceedings of the International Conference 'Aviamechanical engineering and transport' (AVENT 2018). Russia: Atlantis Press; 2018. http://www.atlantis-press.com/php/paper-details.php?id=25901633
35. Mucha J, Witkowski W. The Structure of the strength of riveted joints determined in the lap joint tensile shear test. Acta Mech Autom. 2015 Mar 1; 9(1): 44–9. https://doi.org/10.1515/ama-2015-0009
36. Liu C, Li Y, Cheng Y, Zhao A, Du K, Shi Y, et al. Investigation of stress distribution and damage behavior caused by forced installation of a composite bolted joint with a hole-location error. Chin J Aeronaut. 2024 Jan; 37(1): 201–17. https://doi.org/10.1016/j.cja.2023.07.038
37. Żyłka M, Żyłka W, Klukowski K. Technical solutions enabling the physical training of astronauts during long-term stays at space stations. Adv Sci Technol Res J. 2023 Aug 7; 17(4): 36–45. https://doi.org/10.12913/22998624/167935
38. Żyłka M, Żyłka W, Szczerba Z, Biskup M. An original system for controlling the speed of movement of pneumatic drives in rehabilitation devices. Adv Sci Technol Res J. 2023 Feb 1;17(1):124–32. https://doi.org/10.12913/22998624/157250
39. Żyłka M. The experimental determination of the speed of piston rods of two pneumatic cylinders with a synchronizing element. Adv Sci Technol Res J. 2021 Jun 1;15(2):84–9. https://doi.org/10.12913/22998624/135596
40. Żyłka W. Sampling interval selection for 3D surface roughness measurements using the contact method. Adv Sci Technol Res J. 2021 Dec 1;15(4):283–98. https://doi.org/10.12913/22998624/142192
41. Żyłka WM, Potera P. Testing of the light transmittance of industrial varnishes. Adv Sci Technol Res J. 2024 Jun 1;18(3):14–20. https://doi.org/10.12913/22998624/185463
42. Żyłka W, Majka A, Skała P, Szczerba Z, Cieniek B, Stefaniuk I. Impact of degraded aviation paints on the aerodynamic performance of aircraft skin. Materials. 2025 Jan;18(10):2401. https://doi.org/10.3390/ma18102401
43. Wu CE, Lin KH, Juang JY. Hertzian load–displacement relation holds for spherical indentation on soft elastic solids undergoing large deformations. Tribol Int. 2016 May;97:71–6. https://doi.org/10.1016/j.triboint.2015.12.034
44. Fischer-Cripps AC. Introduction to contact mechanics. 2nd ed. New York: Springer; 2007. 221 p. (Mechanical engineering series).
45. Zhu X. Tutorial on Hertz Contact Stress. International Journal of Engineering Science 2011;49: 576–588.
46. Zhupanska OI. Contact problem for elastic spheres: Applicability of the Hertz theory to non-small contact areas. Int J Eng Sci. 2011 Jul 1;49(7):576–88. https://doi.org/10.1016/j.ijengsci.2011.02.003
47. ISO 12996-2013 Mechanical joining – Destructive testing of joints – Specimen dimensions and test procedure for tensile shear testing of single joints. 2013.
48. Lubas M, Witek L. Influence of Hole Chamfer Size on Strength of Blind Riveted Joints. Adv Sci Technol Res J. 2021 Jun 1;15(2):49–56. https://doi.org/10.12913/22998624/135632
49. Witek L, Lubas M. Experimental Strength Analysis of Riveted Joints Using Blind Rivets. J KONES. 2019 Mar 1;26(1):199–206. https://doi.org/10.2478/kones-2019-0024
50. Dobosz M. Wspomagama komputerowo statystyczna analiza wyników badań. Warszawa: Akademicka Oficyna Wydawnicza EXIT; 2001.
51. Lubas M. The visual research of changes in the geometry of a rivet joint for material model effect for simulation riveted joints made of EN AW 5251. Tech. Aut. Mont. 2022;(4):54–64. https://doi.org/10.7862/tiam.2022.4.6